Investigation of Dose Rate Distribution in an Experimental Hall of a RIKEN Accelerator-Driven Compact Neutron Source Based on the ^{9}Be(p, n) Reaction With 7 MeV Proton Injection

Mingfei Yan, Baolong Ma, Takao Hashiguchi, Atsushi Taketani, Chihiro Iwamoto, Yasuo Wakabayashi, Kunihiro Fujita, Takaoki Takanashi, Masato Takamura, Tomohiro Kobayashi, Shota Ikeda, Maki Mizuta, Yujiro Ikeda, and Yoshie Otake

***Abstract*— To characterize the dose rate distribution in an experimental hall of a RIKEN accelerator-driven compact neutron source (RANS) based on the ^{9}Be(p, n) reaction with 7 MeV proton injection, systematical measurements and calculations for neutron and gamma-ray dose rates by GEometry ANd Tracking (GEANT), Particle and Heavy Ion Transport code System (PHITS), and Monte Carlo N-Particle (MCNP) codes were performed. Calculations always underestimated measurements when proton beam loss effect was not considered. Relatively good agreements were observed among the different simulation codes. To explain the underestimations, the additional dominant neutron and gamma-ray sources due to proton beam loss were identified at the position around exit of the drift tube linac (DTL), made of copper, and the beam pipe from quadrupole (Q) magnets to steering (ST) magnets, made of aluminum, from measurements with placing collimators along linac. The beam loss fractions of 2%–3% on copper and 1% on aluminum, respectively, were the most appropriate estimation. In addition, we proposed the possible measures to reduce the measured total dose rate of 3.8 μSv/h at the operator position in the control room, with the addition of a wall at the entrance of experimental hall and extension of borated polyethylene (BPE) at the end of the beam. As a result, the dose rate became 2.5 times lower than the current one.**

***Index Terms*— Compact neutron source, dose rate distribution, dosimeter, Monte Carlo simulation, proton beam loss.**

Manuscript received December 14, 2021; revised December 21, 2021; accepted January 4, 2022. Date of publication January 7, 2022; date of current version February 16, 2022. This work was supported by the Japan Society for the Promotion of Science (JSPS) Fellows through KAKENHI Grant-in-Aid under Grant 18F18763. *(Corresponding author: Mingfei Yan.)*

Mingfei Yan, Takao Hashiguchi, Atsushi Taketani, Chihiro Iwamoto, Yasuo Wakabayashi, Kunihiro Fujita, Takaoki Takanashi, Masato Takamura, Tomohiro Kobayashi, Shota Ikeda, Maki Mizuta, and Yujiro Ikeda are with the Center for Advanced Photonics, RIKEN, Wako 351-0198, Japan (e-mail: mingfei.yan@riken.jp; t.hashiguchi@riken.jp; taketani@riken.jp; chihiro.iwamoto@riken.jp; y.wakabayashi@riken.jp; kunihiro.fujita@riken.jp; takaoki.takanashi@riken.jp; takamura@riken.jp; t-koba@riken.jp; shota.ikeda@riken.jp; maki.mizuta@riken.jp; yikeda@post.j-parc.jp).

Baolong Ma is with the Department of Nuclear Science and Technology, School of Energy and Power Engineering, Xi'an Jiaotong University, Xi'an, Shaanxi 710049, China (e-mail: mabaolong@stu.xjtu.edu.cn).

Yoshie Otake is with the Center for Advanced Photonics, RIKEN, Wako 351-0198, Japan, and also with the Department of Nuclear Science and Technology, School of Energy and Power Engineering, Xi'an Jiaotong University, Xi'an, Shaanxi 710049, China (e-mail: yotake@riken.jp).

Color versions of one or more figures in this article are available at https://doi.org/10.1109/TNS.2022.3141130.

Digital Object Identifier 10.1109/TNS.2022.3141130

I. Introduction

THE RIKEN accelerator-driven compact neutron source (RANS) has applications in scientific research as well as engineering, such as nondestructive inspection of bridges and highways [1]–[6]. At present, configurations of RANS and RANS-II, a more compact version of RANS, are assembled in the same experimental hall, which has the dimensions of approximately 25 m length and 17.5 m width. The accelerator, RANS target station (TS), experimental sample, and detector are located in the same room. Ideally, TS is equipped with shields that are designed for good shielding performance; however, there is possibility of this configuration creating background radiation, such as radiation leakage from cracks, particularly after recent redesign and assembly. The proton linac is located in the same room, which may lead to an increase in radiation due to proton beam loss. In planning experiments, the characteristics of radiation field from neutrons and gamma-rays need to be identified, especially at the position of the experimental sample. When the RANS control room is located next to the experimental hall, the radiation level for operators in the control room also should be confirmed from a radiation safety perspective. There are several studies about dose rate distribution in the spallation neutron source facilities [7]–[9]; however, there are almost no reports about dose rate investigation associated with compact neutron sources, particularly when the accelerator and beam extraction configuration are located in the same room, where the beam loss could be the possible additional source contributing to background.

Considering the motivations above, a program was conducted to measure the neutron and gamma-ray dose rate distributions in the RANS experimental hall systematically. Three groups of positions throughout the whole experimental hall were measured by neutron and gamma-ray dosimeters. In parallel to those measurements, calculations corresponding to the experimental conditions were performed using the GEometry ANd Tracking (GEANT) [10] code. For cross-checking the simulation results, the Particle and Heavy Ion Transport code System (PHITS) [11] and the Monte Carlo N-Particle (MCNP) [12] codes were also used. Based on comparisons of simulations and experiments, possible radiations

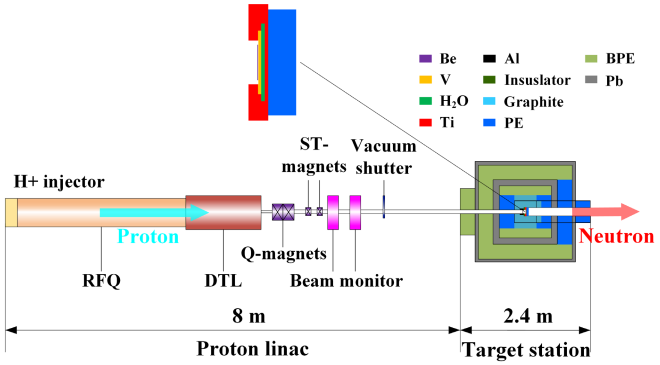

Fig. 1. RANS configuration.

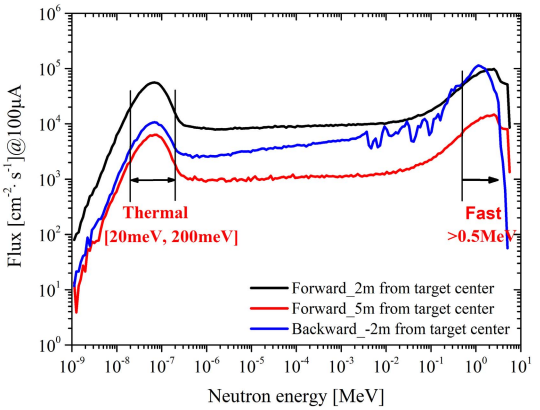

Fig. 2. Neutron energy spectra at different positions simulated by GEANT.

from accelerator components due to proton beam loss were predicted. To prove the prediction, the beam loss positions were identified by measurements by placing collimators along the accelerator. Furthermore, the beam loss fractions were estimated by considering the agreements between simulations and experiments. In addition, to further reduce the radiation level in the control room, addition and extension of shielding structures were proposed.

II. Experiment

A. RANS Configuration

RANS generates neutrons through 7 MeV protons bombardment of a 300-μm thick beryllium (Be) target. As shown in Fig. 1, the proton linac and the TS are the main components. The proton linac is composed of a radio frequency quadrupole (RFQ) section and a drift tube linac (DTL) section. The RFQ accelerates the proton up to 3.5 MeV, while the DTL accelerates the proton from 3.5 to 7 MeV. The proton beam is focused on a 2-cm diameter spot through three quadrupole (Q) magnets. The beam direction can be adjusted through steering (ST) magnets. The maximum average current is 100 μA so that the neutron yield from Be (p, n) reaches 10^{12} n/s [13]. The TS consists of a neutron production target, to which Be is attached on a vanadium (V) substrate; a titanium (Ti) cavity as a water-cooling structure; a polyethylene (PE) moderator; graphite reflectors; and multilayered shields with PE and borated PE (BPE), along with lead. Fig. 2 shows the neutron energy spectra at the positions of -2 m (backward), 2, and 5 m (forward) away from the TS center, with a 4-cm thick moderator. The spectrum at 2 m position shows that the thermal neutron and fast neutron intensities are approximately 8.1×10^5 and 1.6×10^6 cm^{-2}·s^{-1}, respectively. The fast neutron intensity at 5 m position is about six times lower than that at 2 m. The fast neutron energy peak at -2 m position shifts from 2 to 1 MeV, and thermal neutron intensity becomes about six times lower, compared with those at 2 m.

B. Dose Rates Measurement

1) Measurement Positions: As shown in Fig. 3, the whole experimental hall consists of the RANS hall, the RANS-II hall, and the control room, where the RANS-II hall and the

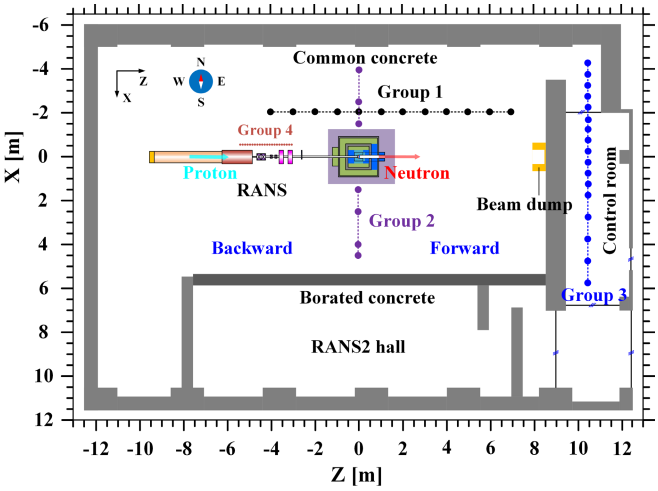

Fig. 3. Measurement positions in the RANS hall and the control room.

control room are located to the south and the east of the RANS hall, respectively. The size of whole hall is approximately 25 m (L) $\times$ 17.5 m (W) $\times$ 7.4 m (H). All walls outside of the building are made of common concrete, whereas the RANS and RANS-II halls are separated by 52-cm-thick borated concrete. A beam dump is assembled upstream of the neutron beam to reduce neutron and gamma-ray background from the wall (92 cm thick) between the RANS hall and the control room. We mainly selected 36 positions, which were categorized into three groups numbered from 1 to 3, for obtaining dose rate distribution in the RANS hall and the control room. The motivations of selected positions are listed in Table I. Additionally, a number of additional positions in group 4, which are located around the proton linac, were measured to identify the proton beam loss positions, which will be further explained in Section IV-B.

2) Detectors for Neutron and Gamma-Ray Dose Rates Measurement: A neutron dosimeter (Hitachi: Aloka TPS-451C) [14] equipped with a ^{3}He proportional counter tube, was applied to measure neutron dose rate. According to the specifications, it has a wide sensitive energy range from thermal neutron to 15 MeV fast neutron, as well as low sensitivity to gamma-rays. Notably, the dosimeter always

TABLE I
MAIN POSITIONS SELECTED FOR DOSE RATE MEASUREMENTS

Groups	LOCATIONS	Motivations
1	RANS hall: 2 m away from beam center north of TS.	Evaluate the shielding performance of TS.
2	RANS hall: cross TS center from the north to the south.	Evaluate the shielding performance of TS.
3	RANS hall & Control room: 1.1 m away from wall between RANS hall and control room.	Evaluate radiation level to confirm the security of operators.

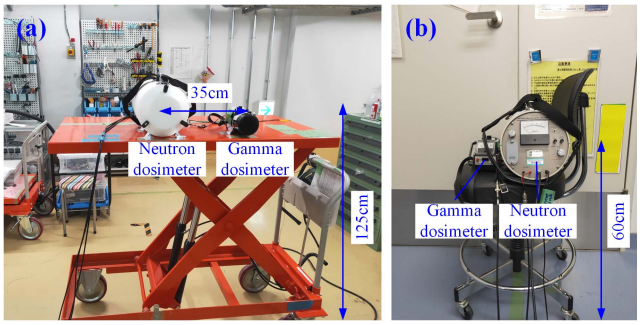

Fig. 4. Detector setups in (a) RANS hall and (b) control room.

over responds in the intermediate energy region, but its effect on the dose rate is limited because the dose rate is dominated by high-energy neutrons. The range of neutron dosimeter is 0.01 μSv/h–10 mSv/h. The gamma-ray dosimeter (Applied Engineering Inc.: AE-133V) [15], which is equipped with an ionization chamber, was applied to measure the gamma-ray dose rate. Given by the specifications, it is sensitive to gamma-ray energy ranging from 30 keV to 2 MeV. The range of gamma-ray dosimeter is 0.1 μSv/h–1000 mSv/h. The quantity that both dosimeters measured is ambient dose equivalent [$H \times (10)$]. Fig. 4(a) and (b) show the measurement setups in the RANS hall and the control room, respectively. The dosimeters were set on a platform of 125 cm height from the floor when measuring the dose rates in the RANS hall, which was the same height of beam center. The dosimeters were set on a chair of 60 cm height from the floor when measuring the dose rates in the control room.

Although, in principle, dose rates can be directly obtained from the display via a remote camera, we recorded the output voltages available in the dosimeters as corresponding dose rates with smaller margin of random error. The steps for calibrating the neutron and gamma-ray dosimeters are as follows: 1) calibrated the relationship between dose rates and output voltages and 2) used another well-calibrated dosimeter as the standard, set at almost same position as the RANS dosimeter, and calculated the calibration factor by comparing the dose rates of both dosimeters as the proton beam current changes. Figs. 5(a) and 6(a) show relationships between the dose rates and output voltages for neutron and gamma-rays, respectively. Their relationships were fitted by exponential and linear functions, respectively. Figs. 5(b) and 6(b) show comparisons of the dose rates of the both dosimeters for neutron and gamma-ray, respectively, as the beam current changed. As a

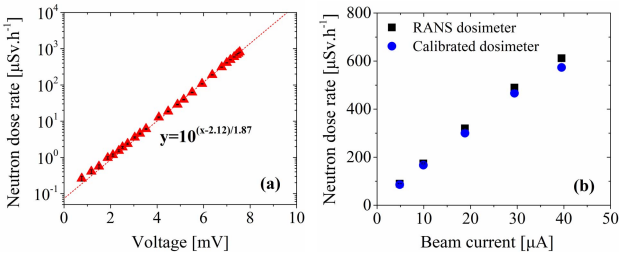

Fig. 5. (a) Voltage-dose rate and (b) beam current-dose rate in calibration of neutron dosimeter.

result, calibration factors of the RANS neutron and gamma-ray dosimeters are 0.98 and 1, respectively, compared with the calibrated dosimeters. Notably, the neutron dosimeter is still not saturated when the dose rate reaches 600 μSv/h, whereas some degree of saturation was observed for the gamma-ray dosimeter when the dose rate reaches 100 μSv/h, as shown in Fig. 6(a). Therefore, the beam current requires to be carefully set to avoid saturation of the gamma-ray dosimeter.

III. SIMULATION

To better understand and evaluate the reliability of measured dose rates at different positions, we performed simulations using the GEANT code according to the experimental conditions. The PHITS and the MCNP simulations were also conducted for comparison.

A. Simulation Conditions

Geometries of RANS including the proton linac, RANS hall including the beam dump, RANS-II hall, and the control room were modeled as closely to the real facility as possible. The dimensions were taken from the design data and real measurements. Notably, RFQ and DTL were simplified as cylindrical tubes in the model without considering their inner structures. The outer diameter of RFQ is 52 cm with 1 cm thick steel wall, while the outer diameter of DTL is 62 cm with 1 cm thick steel wall. The material density and fraction of components, such as common concrete and borated concrete, were employed as described in the design specifications. The default cross section libraries, ENDF/B-VII.1, JENDL-4.0, and ENDF/B-VII.1 for the GEANT4.10.5.1, the PHITS2.52, and the MCNP6.1.1, respectively, were used in the simulations. "QGSP_BERT_HP" package was set as the physics list in the GEANT simulation, while the default physical models were used in the PHITS and the MCNP simulations. As many thermal scattering kernels of $S(\alpha, \beta)$ [16] as available were applied for the specified materials, such as PE and graphite, in the three codes. For the dose map calculation, the whole experimental hall including the control room was divided into 275 (Z) $\times$ 185 (X) $\times$ 1 (Y) meshes, where the height of the mesh center was 125 cm from the floor, and the size of each mesh was 10 cm $\times$ 10 cm $\times$ 10 cm. To save time, the calculation started from the neutron and gamma-rays generated at the Be target via the ^{9}Be(p, n)^{9}B reaction. An energy-dependent angular distribution for neutrons was calculated by a function [17], and an isotropic angular distribution with

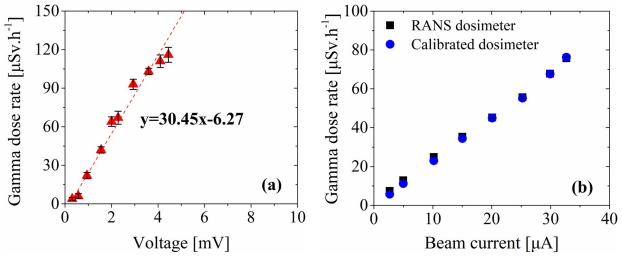

Fig. 6. (a) Voltage-dose rate and (b) beam current-dose rate in calibration of gamma-ray dosimeter.

3.562 MeV mono-energy for gamma-rays was assumed [18]. The dose rate was calculated by combining the energy spectrum and fluence to dose equivalent conversion coefficients, where the same conversion coefficients [19] were utilized among the three codes in these simulations.

B. Dose Map Calculation by GEANT

A function for calculating ambient dose equivalent is not available in the GEANT code at present. A few researchers reported a method for calculating the dose map using the so-called "Scorer" tally in the GEANT [20], [21]. They changed the inner functions by incorporating the fluence to dose equivalent conversion coefficients into the "Scorer" tally. Unfortunately, their codes are not open access and are limited to use. Thus, we developed a method for dose map calculation using the "Scorer" tally without changing any of its functions as follows: 1) "Scorer" tally is called for the first energy bin to calculate particle fluxes for each meshes of the mesh-type detector; 2) repeat step 1) for the second, third, . . . , energy bins until the flux of all the energy bins are calculated; 3) sort the data corresponding to the energy spectra and meshes; and 4) combine the energy spectrum with the fluence to dose equivalent conversion coefficients to obtain the dose map.

Fig. 7(a) and (b) show the calculated neutron and gamma-ray dose maps, respectively, by the GEANT, where the gamma-ray dose rate is mainly contributed by 2.224 MeV hydrogen gamma-rays through neutron capture reactions in PE, BPE, and concrete. In general, the neutron dose rate is much larger than the gamma-ray dose rate in the experimental hall: two orders of magnitude larger at the forward positions, while one order larger at the backward positions. Since neutrons are mainly attenuated by materials containing hydrogen, such as PE, BPE, and concrete, and gamma-rays are strongly absorbed by high-Z materials, such as lead and iron, the neutron and gamma-ray dose maps exhibit different features.

IV. Comparison of the Experiment and Simulation

A. Comparison of Results

We compared the experimental and simulated dose rates at the positions specified in groups 1–3. Fig. 8(a) and (b) show the neutron and gamma-ray dose rate distributions, respectively, for group 1. At the forward positions, the neutron dose rate gradually increased, and a peak appeared at a position around 7 m away from the TS center, according to

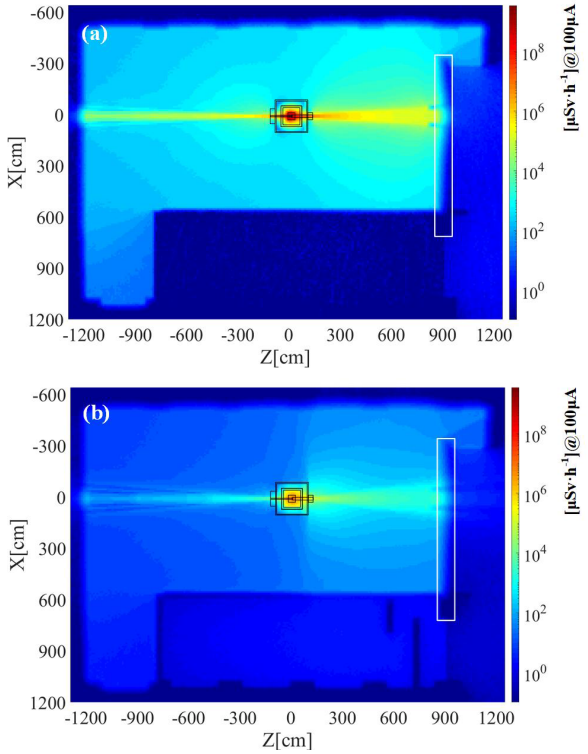

Fig. 7. (a) Neutron and (b) gamma-ray dose maps calculated by the GEANT.

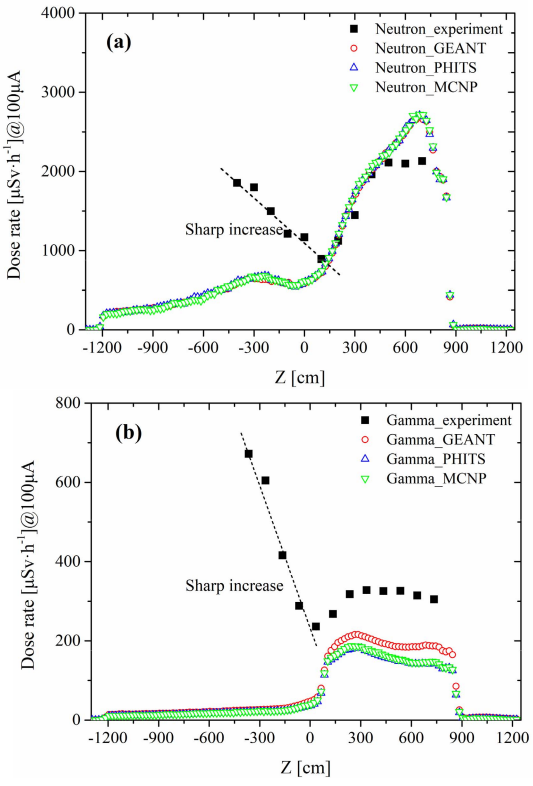

Fig. 8. (a) Neutron and (b) gamma-ray dose rates for group 1.

the calculation. Calculations for neutron dose rates overestimated measurements by approximately 16%–22% from the 600 to 700 cm positions, whereas calculations for gamma-ray dose rates underestimated measurements by 1.5–2.4 times.

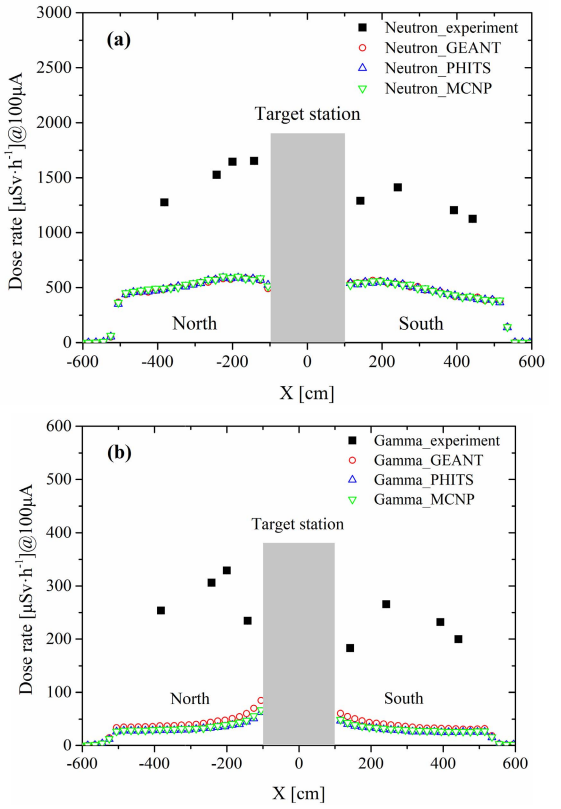

Fig. 9. (a) Neutron and (b) gamma-ray dose rates for group 2.

At the backward positions, sharp increases of both neutron and gamma-ray dose rates were observed in the experiments. Calculations for neutron dose rates were considerably underestimated by 1.9–3.1 times compared with measurements, while gamma-ray dose rates were underestimated by 8.0–35.7 times. Neutron dose rates calculated by the GEANT were almost same as those calculated by the PHITS and the MCNP (with a difference below 3%). However, there were notable differences in gamma-ray dose rates by the three codes, where the GEANT gave the larger estimate, and PHITS and MCNP gave almost the same, but lower. The maximum discrepancy was approximately 30%. It indicated that other radiation sources may have been present around the proton linac part.

Fig. 9(a) and (b) show the dose rate distributions for group 2. Calculations for neutron and gamma-ray dose rates were systematically underestimated compared with measurements. The maximum underestimation factors were approximately 2.4–3.0 for neutron and 3.8–10.1 for gamma-rays. Gamma-ray dose rates calculated by the GEANT were approximately 20% larger than the PHITS and the MCNP. It is notable that the measured dose rates, especially gamma-ray dose rates, increased and then decreased as the distance from TS increased, but the calculated gamma-ray dose rates continuously decreased. It indicated that other gamma-ray sources may have been present during the experiment.

B. Possible Radiations From Accelerator Components Due to Proton Beam Loss

Section IV-A suggested that there were considerably large contributions from accelerator components. According to [22] and [23], such contributions may come from proton beam losses along the linac, which could be additional neutron and gamma-ray sources, leading to an increase of background in the experimental hall. Thus, further investigations were performed to identify the exact beam loss positions and beam loss intensities parametrically.

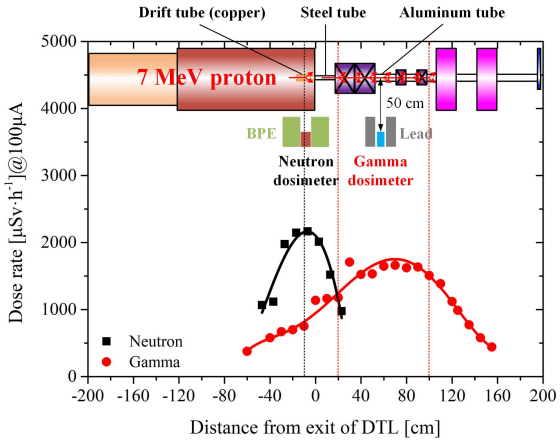

Fig. 10. Investigation of proton-induced radiation sources.

As shown in the upper side of Fig. 10, collimators made of BPE and lead bricks for restricting neutron and gamma-rays, respectively, were used in measuring the dose rates at positions in group 4 with a 10-cm step, to specify the beam loss positions. As a result, additional neutron source was identified at the position of −10 cm from the exit of DTL; the additional gamma-ray source was broadly distributed at positions of around 20–100 cm from the exit of DTL, which was around the Q and ST magnets, as shown in the bottom side of Fig. 10.

The exit of DTL was constructed with drift tubes made of copper surrounded by a vacuum chamber made of steel. The proton beam was transported through steel and aluminum beam pipes, as indicated in the upper side of Fig. 10. Radiations were generated mainly by the (p, n) and (p, γ) reactions when proton beam reacted with those materials. Fig. 11 depicts the cross sections of the reactions for copper, iron, and aluminum with respect to proton energy [24]. Cross sections of the (p, n) reactions for ^{63}Cu, ^{65}Cu, ^{56}Fe, and ^{27}Al were 277, 548, 159, and 28 mb, respectively, with 7 MeV proton, while cross sections of the (p, γ) were 0.33, 0.52, 0.35, and 0.21 mb, respectively. In consideration of position and amounts of materials, along with corresponding cross sections, copper and aluminum were anticipated to be the dominant materials contributing to radiations around the exit of DTL and around the Q and ST magnets, respectively.

To quantitatively estimate the effect of additional radiations, neutron and gamma-ray dose rate distributions were calculated by assuming different fractions of beam losses at the copper and aluminum positions identified by the measurements. In the simulation model (the upper side of Fig. 10), one additional source was described as proton interaction with a thin copper plate at the position of −10 cm; the other one was described as proton interaction with aluminum thin plates broadly distributed at seven positions of 20–100 cm with a 10-cm step.

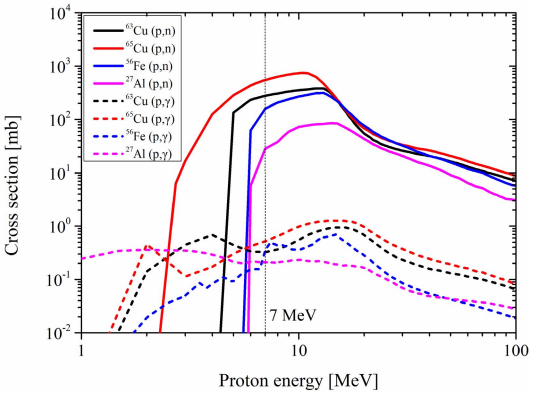

Fig. 11. Cross sections of (p, n) and (p, γ) reactions for copper, iron, and aluminum.

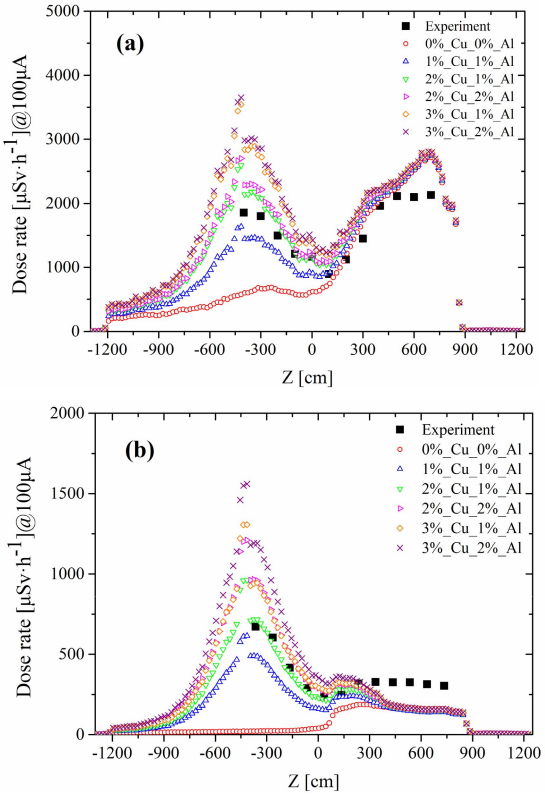

Fig. 12. (a) Neutron and (b) gamma-ray dose rates for group 1, assuming different combinations of beam loss fractions on Cu and Al.

Fig. 12(a) and (b) show comparisons of the PHITS calculations and measurements for neutron and gamma-ray dose rates, respectively, for group 1, assuming different combinations of beam loss fractions for Cu and Al, respectively. It indicates that the contribution of the beam loss in the forward region was small, and dose rates substantially increased in the region along the proton beam line. As can be seen, combinations of 2% Cu and 1% Al (labeled as "2%_Cu_1%_Al") and 2% Cu and 2% Al (labeled as "2%_Cu_2%_Al") suggest that copper was the dominant contribution material for neutron dose rates, while both copper and aluminum were the dominant contribution materials for gamma-ray dose rates. As a result,

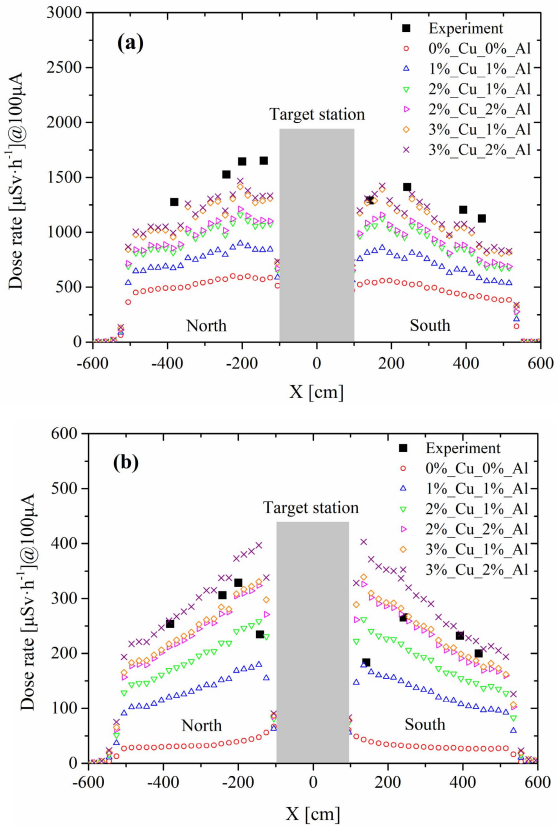

Fig. 13. (a) Neutron and (b) gamma-ray dose rates for group 2, assuming different combinations of beam loss fractions on Cu and Al.

"2%_Cu_1%_Al" was the most probable beam loss estimation. Notably, there was significant underestimation in the calculations for gamma-ray dose rates at the forward positions after 300 cm from the TS center. The underestimation is to be discussed later.

Fig. 13(a) and (b) show the comparisons for group 2, assuming different beam loss fractions. It indicates that "3%_Cu_1%_Al" was an appropriate estimation, as it almost gave the reasonable agreements between the calculations and measurements. In particular, the measured gamma-ray dose rates increased at positions of −100 to −200 cm and then gradually decreased from −200 cm to the wall at the north, and a similar tendency at the south was also observed. Calculations with beam losses could reproduce such a tendency. It was well explained by that the TS shielded some of the additional radiations due to the beam losses. This also confirms that there were beam loss contributions in the dose rate distributions.

V. Reduction of Dose Rates in the Control Room

To confirm the radiation safety of operators, we have evaluated the dose rate level in the control room, where the positions start from the corner of the RANS hall entrance to the other side of the control room. As shown in Fig. 14, dramatic decreases of both the neutron and gamma-ray dose rates were observed at positions around the corner of the RANS hall entrance. After the door, made of iron, dose rates decreased gradually as the distance from the door increased.

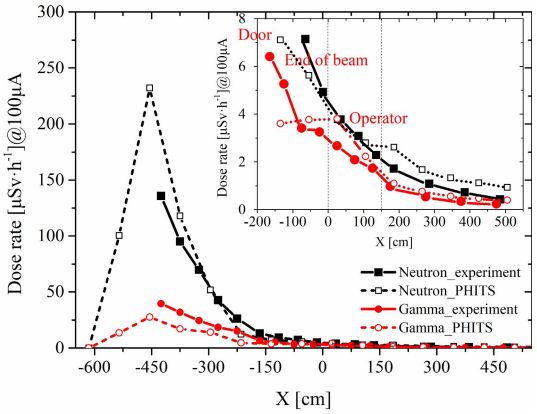

Fig. 14. Neutron and gamma-ray dose rates for group 3.

TABLE II

DOSE RATE REDUCTION BY ADDING AN ADDITIONAL WALL AND BPE ([μSv/h] AT 100 μA)

	Neutron	Gamma-ray	Total
Without additional wall and BPE	2.8	1.7	4.5
With additional wall and BPE	0.9	0.9	1.8
Reduction factor	3.1	1.9	2.5

Although noticeable differences between the measurements and calculations for both neutron and gamma-ray dose rates were observed, the measured neutron and gamma-ray dose rates at the operator position were 2.3 and 1.5 μSv/h, respectively, which resulted in a 3.8-μSv/h total dose rate. It was felt to be high for operators who stay in the control room for long time.

To further reduce the dose rate level in the control room, additional shields are necessary. Before proposing the shielding scheme, we first investigated the sources contributing to neutron and gamma-ray dose rates by filling the entrance of RANS hall with a concrete wall (shown in Fig. 15). As shown in Fig. 16, the neutron dose rate came mainly from the hall entrance, while the gamma-ray dose rate came mainly from the wall at the end of the neutron beam. Then we proposed a wall [200 cm (length) $\times$ 52 cm (thickness) $\times$ 600 cm (height)] around the entrance to reduce the neutron dose rate, and 10 cm thick BPE inside the beam dump and on the wall around the beam dump (50 cm width), respectively, to reduce the gamma-ray dose rate, shown in Fig. 15. As a result, neutron dose rate at the operator position decreased from 2.8 to 0.9 μSv/h, while gamma-ray dose rate decreased from 1.7 to 0.9 μSv/h, resulting in total dose rate decreased from 4.5 to 1.8 μSv/h, shown in Table II. It means that total dose rate can be reduced by a factor of 2.5.

VI. DISCUSSION

Although good agreements between the measurements and calculations were observed for neutron dose rates when including the beam loss effect, calculations of the gamma-ray dose rates at the forward positions after 300 cm from the TS center

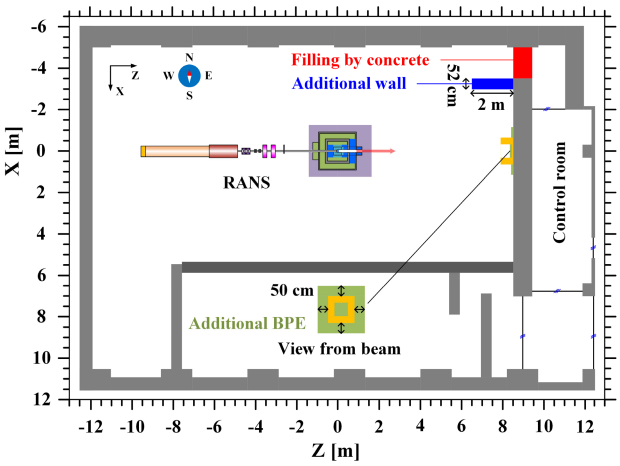

Fig. 15. Experimental hall with the entrance filled, the additional wall, and BPE, respectively.

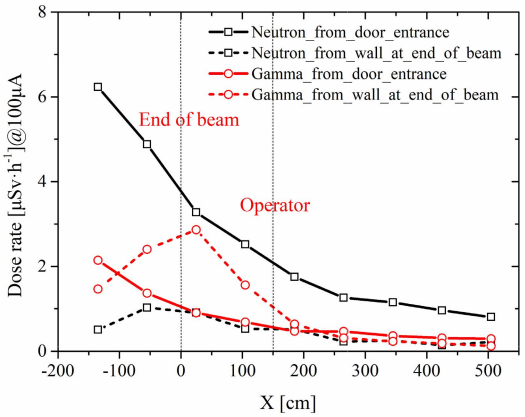

Fig. 16. Dominant sources contributing to neutron and gamma-ray dose rates in the control room.

TABLE III

SIMULATED GAMMA-RAY DOSE RATES WITH DIFFERENT THICK STEEL SUPPORT ([μSv/h] AT 100 μA)

Positions	0 mm	2 mm	10 mm
Group 1: Z=735 cm	137	154	185
Group 2: X=275 cm	29	34	45

for group 1 underestimated the measurements by a factor of 2, shown in Fig. 12(b). To understand the underestimation, we further investigated the effect of materials near the gamma-ray dosimeter, such as the steel support [Fig. 4(a)]. Table III shows the simulated gamma-ray dose rates with different support thicknesses. The influence of the steel support could partially explain the discrepancy between the measurements and calculations. As gamma-ray dose rates measured are mainly from prompt gamma-rays, which show wider range and complex spectra, imperfect energy response of the dosimeter to treat the spectra could be another reason leading to the discrepancy. It is worth mentioning that the gamma-ray dose rates are much smaller than the neutron dose rates at most of

the measured positions. From the total dose rate perspective, such discrepancy is not crucial in current study. However, it should be investigated in future.

In addition, noticeable differences for gamma-ray dose rates were also observed between the GEANT and the PHITS (MCNP), such as at the positions for group 1 shown in Fig. 8(b). There are two most likely reasons: one is the difference in cross section libraries; the other is the difference in physics models to treat production of neutron-induced gamma-rays. Although the GEANT and the MCNP used the same ENDF/B-VII.1 cross section library in our study, the calculated gamma-ray dose rates were different. It suggested that the discrepancy was not mainly from the difference in cross section libraries. According to the report [25] from GEANT developers, it may come from the difference in physics model in different codes.

VII. Conclusion

Systematic measurements and calculations for neutron and gamma-ray dose rates in the RANS experimental hall were conducted. The following conclusions were reached.

(1) Calculations without the proton beam loss always underestimated measurements by 1.5–35.7 times at different positions, in particular backward, measured throughout the RANS hall.
(2) Additional radiation sources due to the proton beam loss were identified as appreciably large, which contributed to the underestimation.
(3) There were two dominant beam loss sources. One was copper located at the exit of DTL, which mainly contributed to the additional neutron dose rate. The other was aluminum beam pipe distributed along a line from the Q magnets to the ST magnets, which mainly contributed to the additional gamma-ray dose rate. The beam loss fractions of 2%–3% on copper and 1% on aluminum, respectively, were estimated to be the most appropriate.
(4) Calculations of the neutron dose rates by the GEANT, PHITS, and the MCNP agreed well (<3%), while the GEANT gave systematically higher by 30% at most than the PHITS and the MCNP.
(5) To further reduce the dose rate level in the control room, it was effective to add an additional wall around the entrance and BPE around the wall at the end of neutron beam.

Our study clearly demonstrated that the beam loss must be considered in dose rate evaluation when the accelerator is located in the same room of the TS. It gives a possible guide for building design of neutron source facilities.

References

[1] Y. Otake, "RIKEN compact neutron systems with fast and slow neutrons," *Plasma Fusion Res.*, vol. 13, Oct. 2018, Art. no. 2401017.
[2] Y. Otake, "RIKEN accelerator-driven compact neutron systems," in *Proc. EPJ Web Conf.*, vol. 231, Feb. 2020, p. 01009.
[3] T. Kobayashi, S. Ikeda, Y. Otake, Y. Ikeda, and N. Hayashizaki, "Completion of a new accelerator-driven compact neutron source prototype RANS-II for on-site use," *Nucl. Instrum. Methods Phys. Res. A, Accel. Spectrom. Detect. Assoc. Equip.*, vol. 994, Apr. 2021, Art. no. 165091.
[4] Y. Ikeda *et al.*, "Prospect for application of compact accelerator-based neutron source to neutron engineering diffraction," *Nucl. Instrum. Methods Phys. Res. A, Accel. Spectrom. Detect. Assoc. Equip.*, vol. 833, pp. 61–67, Oct. 2016.
[5] Y. Seki *et al.*, "Fast neutron transmission imaging of the interior of large-scale concrete structures using a newly developed pixel-type detector," *Nucl. Instrum. Methods Phys. Res. A, Accel. Spectrom. Detect. Assoc. Equip.*, vol. 870, pp. 148–155, Oct. 2017.
[6] B. Ma *et al.*, "Shielding design of a target station and radiation dose level investigation of proton linac for a compact accelerator-driven neutron source applied at industrial sites," *Appl. Radiat. Isot.*, vol. 137, pp. 129–138, Jul. 2018.
[7] F. Masukawa *et al.*, "Neutron dose rate measurements in J-PARC MLF," *Prog. Nucl. Sci. Technol.*, vol. 3, pp. 76–78, 2012.
[8] D. D. DiJulio *et al.*, "Characterization of the radiation background at the spallation neutron source," *J. Phys., Conf.*, vol. 746, Sep. 2016, Art. no. 012033.
[9] Q. Li *et al.*, "Neutron and background measurements of the experimental halls at the CSNS back-streaming white neutron source," *Nucl. Instrum. Methods Phys. Res., Sect. A*, vol. 980, no. 11, Nov. 2020, Art. no. 164506.
[10] J. Allison *et al.*, "Recent developments in Geant4," *Nucl. Instrum. Methods Phys. Res. Section A, Accel., Spectrometers, Detect. Assoc. Equip.*, vol. 835, pp. 186–225, Nov. 2016.
[11] T. Sato *et al.*, "Features of particle and heavy ion transport code system (PHITS) version 3.02," *J. Nucl. Sci. Technol.*, vol. 55, no. 6, pp. 684–690, Nov. 2018.
[12] T. Goorley, "MCNP6.1.1-beta release notes," Los Alamos Nat. Lab., NM, USA, Tech. Rep. LA-UR-14-24680, 2014.
[13] Y. Yamagata *et al.*, "Development of a neutron generating target for compact neutron sources using low energy proton beams," *J. Radioanal. Nucl. Chem.*, vol. 305, no. 3, pp. 787–794, Mar. 2015.
[14] J. Saegusa, M. Yoshizawa, Y. Tanimura, M. Yoshida, T. Yamano, and H. Nakaoka, "Evaluation of energy responses for neutron dose-equivalent meters made in Japan," *Nucl. Instrum. Methods Phys. Res. A, Accel. Spectrom. Detect. Assoc. Equip.*, vol. 516, no. 1, pp. 193–202, Jan. 2004.
[15] AE-133V. *Applied Engineering*. Accessed: Mar. 2021. [Online]. Available: https://www.o-yo-giken.co.jp/AE 133Vcatalog.html
[16] H. N. Tran *et al.*, "Comparison of the thermal neutron scattering treatment in MCNP6 and GEANT4 codes," *Nucl. Instrum. Methods Phys. Res. A, Accel. Spectrom. Detect. Assoc. Equip.*, vol. 893, pp. 84–94, Nov. 2018.
[17] Y. Wakabayashi *et al.*, "A function to provide neutron spectrum produced from the 9Be + p reaction with protons of energy below 12 MeV," *J. Nucl. Sci. Technol.*, vol. 55, no. 8, pp. 859–867, Mar. 2018.
[18] J. Räisänen, T. Witting, and J. Keinonen, "Absolute thick-target γ-ray yields for elemental analysis by 7 and 9 MeV protons," *Nucl. Instrum. Methods Phys. Res. Sect. B, Beam Interact. Mater. At.*, vol. 28, no. 2, pp. 199–204, Oct. 1987.
[19] *Conversion Coefficients for Use in Radiological Protection Against External Radiation*, ICRP, Stockholm, Sweden, vol. 26, 1996.
[20] S. B. Jack, "Monte Carlo simulations and measurements of the radiation environment at a laser-plasma accelerator," M.S. thesis, Lund Univ., Lund, Sweden, Oct. 2016.
[21] N. MacFadden and C. Gulliford Geant, "Development and validation of a Geant4 radiation shielding simulation framework," Brookhaven Nat. Lab., Upton, NY, USA, Tech. Rep. BNL-211700-2019-TECH, CBETA/034, Nov. 2018.
[22] V. Talanov *et al.*, "Neutron doses due to beam losses in a novel concept of a proton therapy gantry," *J. Phys., Conf.*, vol. 874, Jul. 2017, Art. no. 012107.
[23] J. Fernández-Tejero *et al.*, "Beam-loss damage experiment on ATLAS-like silicon strip modules using an intense proton beam," *Nucl. Instrum. Methods Phys. Res. A, Accel. Spectrom. Detect. Assoc. Equip.*, vol. 958, Apr. 2020, Art. no. 162838.
[24] N. Soppera, E. Dupont, and M. Fleming. (Sep. 2020). *JANIS Book of Proton-Induced Cross Sections*. [Online]. Available: https://www.oecd-nea.org/janis
[25] E. Mendoza, D. Cano-Ott, T. Koi, and C. Guerrero, "New standard evaluated neutron cross section libraries for the GEANT4 code and first verification," *IEEE Trans. Nucl. Sci.*, vol. 61, no. 4, pp. 2357–2364, Aug. 2014.